ACS APPLIED MATERIALS & INTERFACES

Research Article

Cite This: ACS Appl. Mater. Interfaces 2019, 11, 1274−1282

www.acsami.org

Consecutively Strong Absorption from Gigahertz to Terahertz Bands of a Monolithic Three-Dimensional Fe_3O_4/Graphene Material

Honghui Chen,[†] Zhiyu Huang,[†] Yi Huang,[*,†] Yi Zhang,[‡] Zhen Ge,[†] Wenle Ma,[†] Tengfei Zhang,[†] Manman Wu,[†] Shitong Xu,[§] Fei Fan,[§] Shengjiang Chang,[§] and Yongsheng Chen[†]

[†]National Institute for Advanced Materials, Tianjin Key Laboratory of Metal and Molecule Based Material Chemistry, Key Laboratory of Functional Polymer Materials, Collaborative Innovation Center of Chemical Science and Engineering (Tianjin), School of Materials Science and Engineering, and [§]Institute of Modern Optics, Nankai University, Tianjin 300350, China

[‡]Beijing Institute of Aeronautical Materials, Beijing 100095, China

Supporting Information

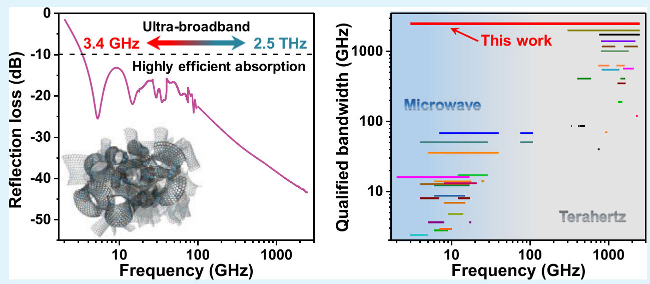

ABSTRACT: With the booming microwave and terahertz technology for communication, detection, and healthcare, the consequently increasingly complicated electromagnetic environment is in urgent need of high-performance microwave and terahertz absorption materials. However, it is still a huge challenge to achieve consecutively strong absorption in both microwave and terahertz regimes. Herein, an ultra-broadband and highly efficient absorber for both microwave and terahertz bands based on the monolithic three-dimensional cross-linked Fe_3O_4/graphene material (3DFG) is first reported. The 3DFG shows an incredible wide qualified absorption bandwidth (with reflection loss less than −10 dB) from 3.4 GHz to 2.5 THz, which is the best result in this area by far. Furthermore, the remarkable absorption performance can be maintained under oblique incidence, different compressive strains, and even after 200 compression/release cycles. The designed highly porous structure for minimizing surface reflection combined with the micro−macro integrated high lossy framework results in the excellent absorptivity, as verified by the terahertz time-domain spectroscopy technique. With these, the 3DFG achieves an unprecedentedly average absorption intensity of 38.0 dB, which is the maximum value among the broadband absorbers. In addition, its specific average microwave and terahertz absorption value is over 2 orders of magnitude higher than other kinds of reported materials. The results provide new insights for developing novel ultra-broadband absorbers with stronger reflection loss and wider absorption bandwidth.

KEYWORDS: *graphene, three-dimensional, electromagnetic wave, terahertz absorption, broadband*

INTRODUCTION

Communication and detection technologies have been profoundly reformed with the booming material and computer science. As the medium of long-distance data transmission, electromagnetic waves in the entire microwave regime have been widely applied in the fields of communication, remote sensing, and radar,[1−3] such as Wi-Fi and military multifunctional integrated radio-frequency system. Especially lately, the tremendous progress in artificial intelligence and consumer electronics makes the technology really step into the millimeter wave band. For instance, 77 GHz radar offers the crucial object detection and ranging for autonomous driving technology,[4] and the high transmission speed requirement of the fifth-generation mobile communications (5G) needs the essential support of millimeter wave technology.[5] Meanwhile, as a next-generation technology for communication and detection, the terahertz (THz) technology is drawing more attention than ever before because of the fascinating prospect in space and short-distance applications.[6] The terahertz band offering very broad bandwidth is identified as one of the promising spectrum bands to enable ultrahigh-speed wireless communications. In addition, the strong penetrating ability, high-range resolution, anti-interference ability, and so forth endow THz radar with great superiority over microwave radar.[7] For example, Schaubert and co-workers developed a terahertz-pulsed radar system for remote-sensing applications, which is capable of making backscatter measurements from terrain targets at ranges of several kilometers.[8] For the detection technology in the foreseeable future, both long-distance and short-distance detecting devices will be equipped to obtain full-scale and high-resolution target information. It is conceivable that the future communication and detection technologies must be multiband integrated ranging from gigahertz to terahertz over extremely broad spectrum range, accompanied by sever electromagnetic pollution, information security, and health and military threats in these regions.[9−12] To this end, it is extremely urgent to

Received: October 9, 2018
Accepted: December 4, 2018
Published: December 4, 2018

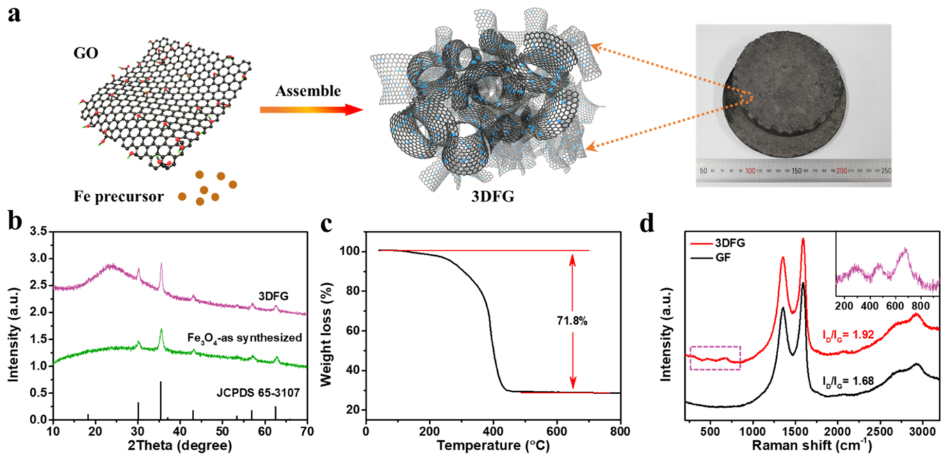

Figure 1. Schematic illustration of the preparation process of 3DFGs. (a) Process of fabricating 3DFGs. (b) X-ray diffraction (XRD) spectra of 3DFGs and Fe_3O_4. (c) Thermogravimetric analysis (TGA) curve of 3DFG annealed at 250 °C. (d) Raman spectra of 3DFG and GF annealed at 250 °C.

develop high-performance electromagnetic wave absorption materials (EAMs) covering both microwave and THz bands for civil applications (e.g., eliminating undesired electromagnetic radiation and manipulating information transportation) and military stealth equipment.[13,14]

Great efforts have been paid to develop new microwave and terahertz absorber with high absorptivity and broad qualified absorption bandwidth [with reflection loss (RL) less than −10 dB].[15] Additionally, maintaining excellent performance under oblique incidence is also of great importance.[16] However, owing to the very large wavelength span, it is extremely challenging to tune the component and structure of the absorber for incredibly broad spectrum absorption. It should be noted that the burgeoning nanomaterial and processing technology further advance the development of EAMs.[17−19] Because most well-designed absorbers with elaborate structures were casually added into matrices as fillers, the intrinsic advantages of particulate structure were overwhelmed by the random distribution of particulate groups and the expected properties could not be fully realized in many cases, thus leading to limited improvement of absorption performance. Beyond that, the large loading content typically brings about high-effective solid contents and refractive index of the composite, which may cause large surface reflection for THz waves, resulting in bad THz absorption performance. Based on the quarter-wavelength matching model, Jaumann screen and circuit analogue structure absorbers are capable of acquiring a relatively wide qualified absorption bandwidth in the microwave region through creating multiple response absorption peaks.[20−22] However, these two structure designs are confronted with the complicated optimization process, and the fussy fabrication procedure for THz absorption is another big issue. Recently, metamaterials (MMs) have been widely investigated as EAMs in microwave and THz regimes.[23,24] Owing to the narrow absorption bandwidth characteristic of most MMs, it has to integrate multiple resonance units with different geometric dimensions or design multilayered size-varied resonance unit structures to obtain multiband or broadband MM absorbers.[25−27] Nevertheless, the dimension of the resonance units designed for microwave and THz frequencies is quite different, ranging from tens of millimeters to a few microns.[6] This greatly increases the difficulty of overall structure design and high precision manufacturing for extremely complicated trans-scale structures, leading to low applicability. Hitherto, to the best of our knowledge, such kinds of EAMs mentioned above, with strong absorption both in microwave and THz bands, have not been reported.

One possible strategy for adapting to the huge difference in wavelength is to integrate general low reflective surface structure with a high lossy skeleton material. In this respect, the porous framework is an ideal structure to reduce effective permittivity and surface reflection for good matching of free space and absorber in both microwave and THz regions. Besides, the porous structure is helpful to increase the wave propagation paths in the absorber, thus promoting the wave attenuation. The widely used honeycomb structural materials and polymer foam-based absorbers have adopted this porous structure.[28−30] A high lossy EAM design is another key point. As a promising two-dimensional carbon nanomaterial, graphene has drawn significant attention in various fields because of its fascinating electrical, optical, and mechanical properties.[31−35] Although a few graphene-based materials have exhibited broad absorption in microwave and THz bands separately, these materials are still suffering from low absorption intensity, weak absorption in low frequency, and relatively narrow qualified absorption bandwidth. It still remains a great challenge to achieve consecutively strong absorption in both microwave and terahertz regimes. The integration of multiple lossy materials with complementary electromagnetic response is probably a feasible route to enhance wave attenuation ability,[36−40] especially in low-frequency band. In addition, the three-dimensional (3D) cross-linked porous lossy structure is conducive to broadening absorption bandwidth.[41,42] Hence, the introduction of magnetic component into the highly porous graphene bulk material to gain a balanced impedance matching and strong attenuation ability over the whole microwave and THz bands may lay the groundwork for the exploitation of desired EAMs.

Herein, we demonstrate an ultralight 3D cross-linked Fe_3O_4/graphene bulk material (3DFG) and achieve consecutive and highly efficient absorption in extremely broad spectrum ranging from gigahertz to THz for the first time. The macroscopic 3DFG exhibits an ultra-broadband qualified absorption bandwidth (from 3.4 GHz to 2.5 THz). Moreover, the designed highly porous cross-linked structure endows the 3DFG still with excellent absorption performance after

DOI: 10.1021/acsami.8b17654
ACS Appl. Mater. Interfaces 2019, 11, 1274−1282

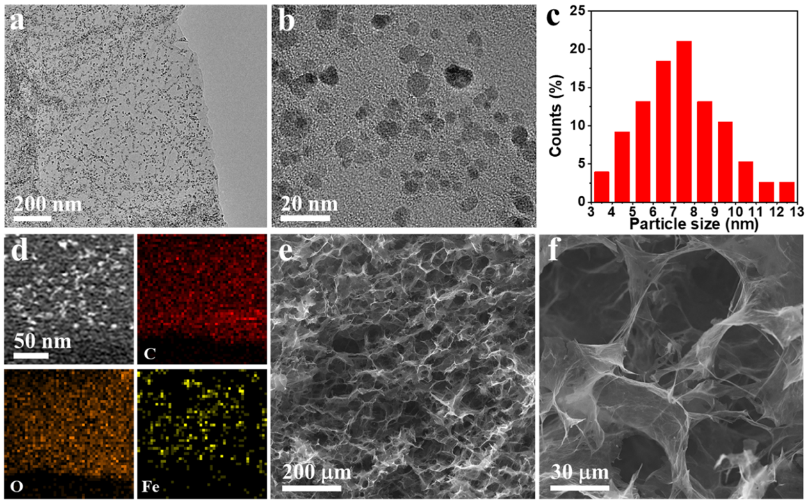

Figure 2. (a,b) TEM images of 3DFGs at different magnifications. (c) Particle size distribution of Fe_3O_4 on graphene sheets. (d) High-resolution TEM image and corresponding EDX mappings of C, O, and Fe. (e,f) Cross-sectional scanning electron microscopy (SEM) images of 3DFGs.

multiple, repeated compression/release cycles, under oblique incidence and different compressive stains. A terahertz time-domain spectroscopy (THz-TDS) technique confirms the negligible surface reflection and strong attenuation of 3DFG for THz waves. More impressively, the 3DFG shows a superb average absorption intensity (AAI) of 38.0 dB, which is the maximum value among the broadband EAMs. In addition, its specific average microwave and THz absorption (SAMTA) value is over 2 orders of magnitude higher than other kinds of EAMs reported to date.

RESULTS AND DISCUSSION

Figure 1a schematically shows the preparation procedure for monolithic 3DFG through a facile solvothermal synthesis of graphene oxide (GO) and Fe precursor, followed by solvent exchange, freeze drying, and annealing process. The abundant oxygen-containing functional groups of GO with lone electron pair can efficiently bind ferric ions to form GO−Fe^{3+} complex, leading to the formation of stable Fe^{3+}/GO colloid solution. Subsequently, the in situ solvothermal process resulted in the growth of Fe_3O_4 nanoparticles within/on the graphene sheets. Choosing ethanol as the reaction medium is of vital importance, the solvothermal process converts GO into reduced GO (RGO), which shows obvious hydrophobicity. The low surface tension of ethanol guarantees the wetting of RGO sheets during the solvothermal process, which reduces the possibility of restacking of RGO sheets. As expected, the obtained 3DFGs exhibit an ultralow bulk density of 2.3 mg cm^{-3} and excellent elasticity during multiple compression/release cycles to 90% strain (Figure S1). For comparison, graphene foams (GFs) were also fabricated using the similar method.

The internal structure of 3DFGs is characterized by XRD, as shown in Figure 1b. The broad diffraction peak centered at 23.6° corresponds to the (002) plane of graphitic carbon, indicating the very weak long-range restacking of graphene sheets. Besides, the observed diffraction peaks well matched with the standard diffraction peaks (JCPDS card no. 65-3107, Fe_3O_4 phase), which confirms the successful transformation from Fe precursor to Fe_3O_4. The characterization X-ray photoelectron spectroscopy (XPS) also gives the consistent results with the XRD pattern (Figure S2). The content of Fe_3O_4 is about 27.3 wt % in 3DFG, as calculated by TGA (TGA, Figure 1c). In addition, the energy-dispersive X-ray spectroscopy (EDX; Figure S3) result shows that the atomic ratio of C/Fe is 12.9, which is similar to the inductively coupled plasma (ICP) analysis (11.3). Raman spectroscopy was further employed to investigate the structural changes of the graphene framework (Figure 1d). The displayed two prominent peaks at 1359 and 1580 cm^{-1} are assigned to the disorder in the graphitic structure (D band) and the in-plane displacement of carbon atoms in hexagonal (G band), respectively. Besides, the additional peaks at 289, 485, and 674 cm^{-1} in 3DFG, corresponding to the E_g, T_{2g}, and A_{1g} vibration modes of Fe_3O_4,[43] respectively, which is consistent with the XRD and XPS results. In addition, the hysteresis loops of 3DFGs also exhibit the magnetic properties of 3DFGs (Figure S4). Obviously, compared to GF, the 3DFG exhibits smaller sp^2 carbon domain, as evident from the higher peak area ratio of D band to G band (I_D/I_G), which is associated with the defect concentration of carbon materials. This is mainly ascribed to the confinement of generated Fe_3O_4 nanoparticles, which occupies the physical and chemical defects of graphene sheets.[44] The consequent enormous multi-interfaces among 3DFG are expected to generate stronger electric dipole, interface polarization, scatter response, and so forth, which are all in favor of electromagnetic wave attenuation.[11,39,44,45]

Transmission electron microscopy (TEM) images of 3DFGs in Figure 2a,b offer more distinct morphology and size distribution of nanoparticles. The nanoparticles are homogeneously distributed throughout the surface of graphene sheets at the nanoscale, as shown in Figures 2a and S5. This evenly distributed feature is mainly attributed to in situ nucleation pattern and abundant oxygen-containing functional groups of GO. The interparticle spacing ranges from a few nanometers to tens of nanometer, and the average size is about 7.4 nm (Figure 2c), according to the measured diameter from 100 particles in Figure S5. EDX mappings also highlight the homogeneous distribution of Fe element in 3DFG (Figure 2d). The confinement of graphene defects may suppress the agglomeration of particles. Nevertheless, the agglomeration of particles will emerge while further raising the content of precursor because of the finite nucleation sites on GO sheets

DOI: 10.1021/acsami.8b17654
ACS Appl. Mater. Interfaces 2019, 11, 1274−1282

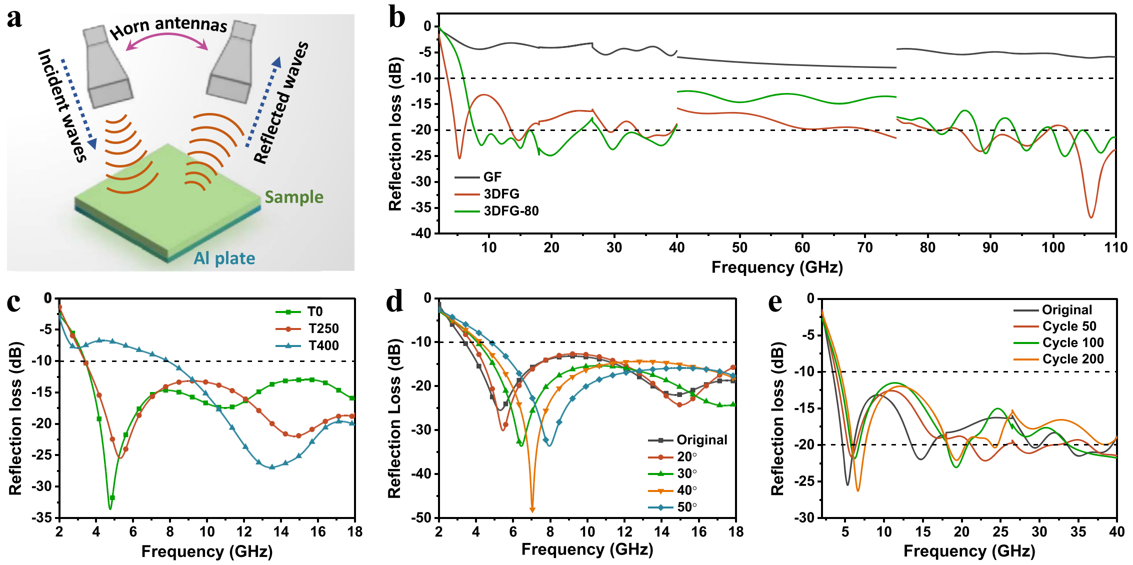

Figure 3. Microwave absorption performance of 3DFGs. (a) Schematic illustration of the measurement by using the Arch method. (b) RL curves of 3DFG, 3DFG under the compressive strain of 80% (3DFG-80), and GF with an annealing temperature of 250 °C in the frequency range of 2–110 GHz. (c) Measured RL curves of 3DFGs with different annealing temperatures in 2–18 GHz; the measured RL curves for 3DFGs with an annealing temperature of 250 °C (d) at various electromagnetic wave incident angles and (e) after different compression/release cycles.

(Figure S6). The graphene sheets within homogeneously distributed Fe_3O_4 nanoparticles can be considered as a flexible 2D Fe_3O_4/graphene sheet (2DFG) building block, and using this 2DFG for building up a monolithic 3DFG with less stacking obviously contributes to maximizing the advantage of Fe_3O_4/graphene for responding to electromagnetic waves and then attenuating them. Indeed, the obtained 3DFG exhibits highly porous structure with pore size ranging from several nanometers to tens of micrometer, as shown in Figures 2e,f and S7. Moreover, the flexible 2DFGs are beneficial to be cross-linked together and thus extend to a huge FG network. These obviously contribute to its excellent elasticity (Figure S1). However, more importantly, the highly porous structure can greatly reduce the effective solid content of the 3DFGs, leading to a low effective permittivity and refractive index over the whole spectrum range,[46] which contributes to the low surface reflection. Therefore, the 3DFG composed of the 2DFGs is expected to achieve a balance between reflection and absorption in both microwave and THz frequency ranges.

The absorption performance of 3DFGs in the microwave regime was first evaluated using the Arch and coaxial-line method. For convenience, the 3DFGs with annealing temperatures of 250 and 400 °C were abbreviated as T250 and T400, respectively. The 3DFG without thermal treatment was labeled as T0. Figure 3a gives the schematic diagram of the Arc method with one horn antenna serving as a signal transmitter and another antenna as a receiver (for details, see the Supporting Information). The 3DFG exhibits an outstanding absorption performance in the whole measured frequency range of 2–40 and 75–110 GHz (Figure 3b). Its AAI (integrated the absolute value of RL divided by the measured frequency range, see the Supporting Information) value exceeds 20 dB, and the measured qualified absorption bandwidth reaches up to 71.6 GHz (3.4–40 and 75–110 GHz), which covers the C (4–8 GHz), X (8–12 GHz), Ku (12–18 GHz), K (18–26.5 GHz), Ka (26.5–40 GHz), W (75–110 GHz), and part of S (2–4 GHz) bands.[47] On the contrary, the GF merely owns the minimum RL value −5.5 dB. The CST simulated curve based on transmission line theory in 18–110 GHz agrees well with the measured result (Figure S8). In addition, the simulated RL results in V band (40–75 GHz) indicate that the 3DFG possesses consistent and strong absorption performance in the whole 2–110 GHz (Figure 3b). Overall, the qualified absorption bandwidth of 3DFG (106.6 GHz) is known to be the widest value among the previously reported materials in this area. Benefiting from the excellent compressive elasticity, we tested the RL values of 3DFG under different compressive strains of 40% (3DFG-40), 60% (3DFG-60), and 80% (3DFG-80) (Figures 3b and S9). Remarkably, even as the 3DFG suffers a compressive strain of 80%, the obtained 3DFG-80 with 2 mm thickness still possesses a qualified absorption bandwidth of 104.1 GHz (5.9–110 GHz) in this area (Figure 3b), demonstrating the tunable thickness of compressible 3DFG while maintaining excellent absorption performance. The annealing process can greatly affect the complex permittivity and absorption performance of graphene-based materials. Too high annealing temperature causes the increase of the reflection of waves and makes the qualified absorption bandwidth of 3DFG narrower (Figure 3c), which is correlated with the increased permittivity of 3DFGs (Figure S10). This may be ascribed to the enlarged interfacial impedance gap caused by the significantly increased C/O ratio and sp^2 carbon domain size as reported before.[42]

Maintaining excellent absorption performance within the wide incident angle is important for real electromagnetic environment. The absorption intensity and qualified absorption bandwidth of most reported MMs decrease significantly at oblique incidence. Instead, the absorptivity of 3DFG remains almost steady at different incident angles (20°, 30°, 40°, and 50°), as shown in Figure 3d. In addition, at the incident angle of 40°, the minimum RL value of 3DFG can reach −48.1 dB at 7.04 GHz. Furthermore, at the incident angle of 50°, the frequency bandwidth with RL less than −15 dB increases by 26% from 9.7 to 12.2 GHz compared with the original results. Subsequently, the RL curves of T250 before and after different compression/release cycles to a high 90% strain were measured

DOI: 10.1021/acsami.8b17654
ACS Appl. Mater. Interfaces 2019, 11, 1274–1282

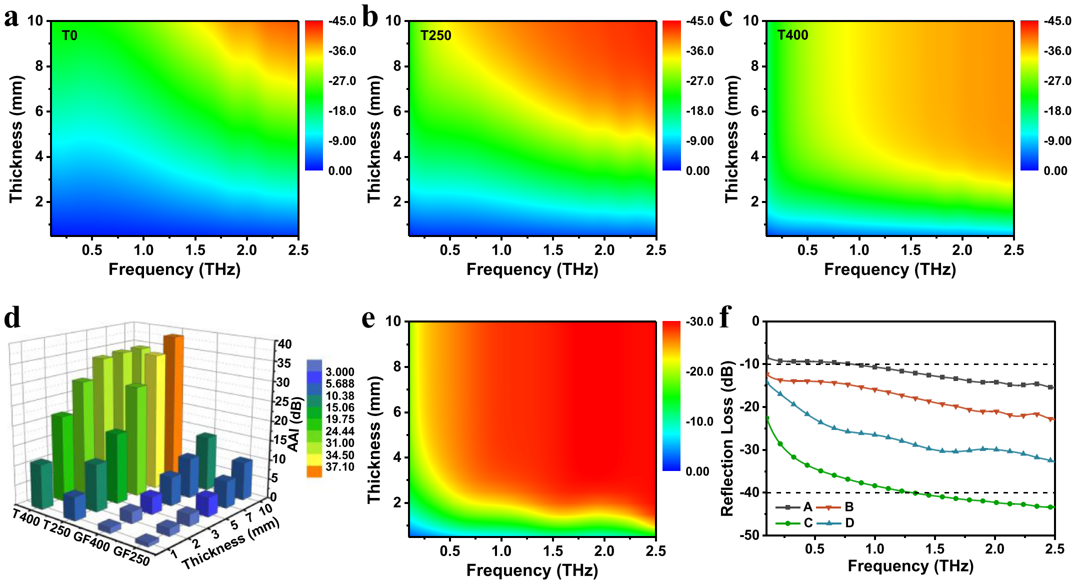

Figure 4. Terahertz absorption performance of 3DFGs. 3D representations of RL values of (a) T0, (b) T250, and (c) T400 in 0.1−2.5 THz. (d) Comparison of terahertz absorption performance for GFs and 3DFGs. (e) 3D representation of RL values of 3DFG-80 in 0.1−2.5 THz. (f) RL values of T250 with (A) 2, (B) 3, (C) 10 mm thickness, and (D) 3DFG-80 with 2 mm thickness.

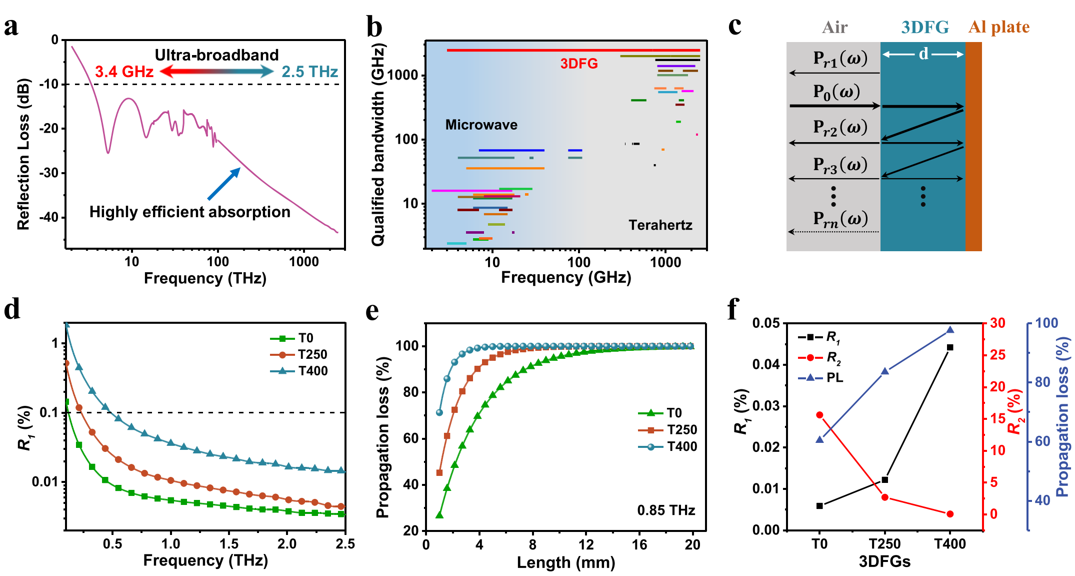

Figure 5. (a) RL curves of T250 in the whole frequency range of 2 GHz to 2.5 THz. (b) Comparison of the qualified absorption bandwidth of represented materials in microwave and terahertz bands. Each color bar with the same qualified bandwidth represents an absorber. A detailed description of each color bar is presented in Table S1. (c) Schematic diagram of the propagation of terahertz waves. (d) R_1 curves of 3DFGs in 0.1−2.5 THz with different annealing temperatures. (e) Plot of propagation loss (PL) of 3DFGs as a function of propagation length at 0.85 THz. (f) R_1, R_2, and PL values of 3DFGs with a sample thickness of 3 mm at 0.85 THz.

(Figures 3e and S11). The qualified absorption bandwidth has almost no shrunk even after 200 compression/release cycles, manifesting the structural stability of the cross-linked 3DFG framework. Consequently, the remarkable absorption performance of 3DFG under normal and oblique incidence, under different compressive strains and after multiple, repeated compression/release cycles enables the high adaptability in complex microwave and physical environment.

The THz region (0.1−10 THz) possesses ultra-wide bandwidth which is nearly 2 orders of magnitude larger than the microwave regime. This put forward higher request on designing and fabricating broadband THz absorber. In addition, the EAMs with high absorptivity in both microwave and terahertz bands have not been reported so far. Aside from the remarkable performance in the microwave region presented above, the 3DFG exhibits surprisingly even better absorption in the THz band. The THz absorption performance of 3DFG in 0.1−2.5 THz was evaluated on a commercial THz-TDS system (for details, see the Supporting Information). On the basis of the detected THz signals (Figure S12), the RL curves of 3DFGs with different annealing temperatures and thicknesses were obtained (Figure 4a−c). Clearly, in contrast to GFs (Figure S13), the corresponding 3DFGs exhibit significantly improved THz absorption performance and the AAI values are obviously greater than that of GFs (Figure 4d). For example, the minimum value of RL reaches −35.0 dB for

T400 with 3 mm thickness, and its qualified absorption bandwidth covers the entire measured frequency range of 0.1−2.5 THz (Figure 4b). In contrast, the RL value of GF400 with the same thickness reaches just −6.8 dB (Figure S13c). Besides, the THz absorption of 3DFG becomes better as its thickness increased because of the longer optical distance (Figure 4a−c). The T250 under the compressive strain of 80% (3DFG-80) demonstrates higher absorptivity with small thickness, as shown in Figure 4e,f, whereas better absorption performance is achieved by T250 than 3DFG-80 at large thickness because of the difference for reflecting terahertz wave from the front surface of the sample, as discussed later. Combined with its excellent absorption performance in the microwave region (2−110 GHz), it can be concluded that both 3DFG and 3DFG-80 samples with 2 mm thickness achieve consecutive ultra-broadband and highly efficient absorption of electromagnetic wave spectrum ranging from gigahertz to THz.

The electromagnetic wave absorption performance of 3DFG shows important advantages over the reported materials, as represented in Figure 5a,b. The optimal 3DFG possesses highly efficient and consistent absorption in extremely broad spectrum ranging from 3.4 GHz to 2.5 THz, which has not been achieved in previous works. In addition, its AAI value (38.0 dB) is the maximum value among the broadband EAMs reported to date, which just exhibit qualified absorption in either gigahertz or THz band separately with mediocre absorption strength (Figure 5b and Table S1). These indicate that the 3DFG has better adaptability in the complex electromagnetic environment. It should be noted that the absorption intensity shows an increasing trend with the blue shift of measured frequency (Figure 5a), indicating that the 3DFG may possess better performance in the higher frequency range. Further integration of its density, qualified absorption bandwidth, and RL values, the SAMTA performance of 3DFG reaches 1.6×10^4 dB g^{-1} cm^3, which is over 2 orders of magnitude higher than other kinds of available materials previously (Figure S14 and Table S1).

The geometry structure of EAM and its attenuation ability for electromagnetic waves greatly determine the absorption performance, which is closely associated with the ratio of reflected wave power to absorbed power. As demonstrated above, the evenly distributed Fe_3O_4 nanoparticles on graphene sheets create enormous multi-interfaces and defects among 3DFG, which contributes to generating sufficient interface polarization, resonance relaxation, scatter response, and so forth for dissipating microwave energy in the heat form. Subsequently, through constructing monolithic 3DFG using the building block of 2DFG sheets, the abundant pores of the size ranging from several nanometers to tens of micrometers can be formed within the 3DFG, which contributes to enhancing multiple scale scattering for microwave, thus leading to the longer wave propagation paths in 3DFG. The active interaction of atomic vibration in disordered material and interband transitions in graphene also endow 3DFG with strong response for THz radiation.[48−50] Therefore, the attenuation for both microwave and terahertz wave can be enhanced at microscale. Besides, the 3D interconnected framework formed by nano−micro lossy units inside the 3DFG could generate induced currents in the pore walls when responding to the propagated electromagnetic waves. Such long-range induced currents can also be intensively decayed by the resistive 3DFG network,[2,51] as can be drawn from the large dielectric loss tangent in the microwave regime (Figure S10) and absorption coefficient in the terahertz regime (Figure S15). Therefore, the vertical integration of wave loss units from nanoscale to microscale and then to macroscale makes 3DFG turn into a high lossy material. On the other hand, the highly porous structure of 3DFG greatly reduces the effective solid content of the 3DFGs, leading to a low real part of permittivity over the whole spectrum range (Figures S10 and S16), which guarantees both appropriate impedance matching characteristic at microwave regime and low surface reflection for incident terahertz waves due to well-matched efficient dielectric contents of 3DFG with that of air at terahertz regime. Eventually, an extraordinary absorption performance ranging from gigahertz to terahertz bands for 3DFG is achieved successfully.

To further understand the excellent performance of 3DFGs, we calculated the power of reflected waves and PL in the THz regime. Figure 5c shows the schematic diagram of the propagation of the THz wave. The incoming power of THz signal can be divided into the power of multiple reflection and absorption, and the transmission is not taken into account for reflection mode. The whole power of reflected THz wave can be represented as

$$E_R{}^2(\omega) = E_{r1}{}^2(\omega) + E_{r2}{}^2(\omega) + E_{r3}{}^2(\omega) + ... + E_{rn}{}^2(\omega) + ... \quad (1)$$

where $E_{r1}(\omega)$, $E_{r2}(\omega)$, $E_{r3}(\omega)$, and $E_{rn}(\omega)$ in eq 1 respond to the electromagnetic field intensity of the first, second, third, and nth reflected THz wave signal from the front surface of the absorber sample, respectively (Figure 5c). We evaluated the PL of THz waves in 3DFGs and the ratio of first (R_1) and second (R_2) reflected THz signal power to incoming power of THz signal of different 3DFGs (for details, see the Supporting Information). As shown in Figure 5d, all of the three 3DFGs show very small average R_1 value (less than 0.1%) in 0.1−2.5 THz, indicating almost no THz reflection from the front surface for incident THz waves, as verified by their ultralow refractive index (Figure S17) and real part of permittivity (Figure S16). This clearly demonstrates that our designed highly porous structure can greatly decrease the surface reflection. On the contrary, most reported EAMs, for instance $BaTiO_3$/polymer nanocomposite (2.26),[52] have a large refractive index. Elevating the annealing temperature, the R_1 values receive a slight increase, demonstrating gradually enlarged surface reflection. The PL reflects the capacity of attenuating THz waves. With the increase of annealing temperature, the PL value of 3DGF is evidently improved (Figure 5e). For example, the PL value at 0.85 THz increased from 46.3% for T0 sample to 91.8% for T400 sample with 2 mm propagation length. This means that elevating annealing temperature obviously contributes to improving the attenuation ability of 3DFG, which can also be drawn from the increased absorption coefficient and extinction coefficient (Figures S15 and S18). In addition, this is also proved by the opposite change trend of R_2 (Figures S19 and S20). Figure 5d exhibits the ability of different 3DFGs for reflecting and attenuating THz waves more intuitively. The T400 shows more efficient absorption in low thickness, whereas T250 and T0 can achieve higher absorptivity with large thickness because of their smaller R_1 values (Figure S21). Besides, the R_1 values are also sensitive to the macroscopic pore structure. The R_1 values can be greatly increased when exerting large compressive strain to 3DFG (Figure S22). For example, the

DOI: 10.1021/acsami.8b17654
ACS Appl. Mater. Interfaces 2019, 11, 1274−1282

T250 under the compressive strain of 95% has adverse R_1 value of 9% at 0.2 THz. There is negative correlation between the optimal thickness at the best performance for 3DFG and its compressive strain (Figure S22). This means that the control of micro−macrostructure can effectively tune the proportion of reflection and absorption and thus the performance of absorber (Figure S23). Therefore, through regulating the annealing temperature, thickness, and porosity of 3DFG, the THz absorption performance can be fine-tuned.

■ CONCLUSIONS

In summary, we have successfully achieved strong and consistent absorption across extremely broad spectral range from gigahertz to terahertz by designing ultralight 3DFG. Compared with the previously reported materials, including MMs, the macroscopic 3DFG exhibits an ultra-broadband qualified absorption bandwidth ranging from 3.4 GHz to 2.5 THz, consecutively. Besides, the excellent elasticity renders its stable absorptivity even after 200 multiple, repeated compression/release cycles. In addition, the 3DFG also exhibits steady absorption performance under oblique incidence and different compressive strains, demonstrating the tunable thickness of absorber while maintaining an excellent absorption performance. Furthermore, the calculated results demonstrate that the highly porous structure can significantly reduce the first reflected THz wave energy, and the micro−macrointegrated high lossy 3DFG network can effectively attenuate the propagated electromagnetic wave, resulting in greatly decreasing the second reflected THz energy. Finally, the 3DFG achieves a remarkable AAI of 38.0 dB, which is the maximum value among the broadband EAMs. In addition, its SAMTA value is over 2 orders of magnitude higher than other kinds of EAMs reported to date. The lightweight 3DFG EAM with strong absorptivity in both microwave and THz bands really opens up the opportunity for increasingly complex electromagnetic environment in life and military detection technology in the future.

■ EXPERIMENTAL SECTION

Fabrication of 3DFGs and GFs. GO sheets were prepared through a modified Hummers' method as described previously.[51] 3DFGs were fabricated through a solvothermal method. Briefly, a certain amount ethanol solution of ferric acetylacetonate was mixed with GO ethanol solution (the concentration of GO in mixed solution was maintained at 1.0 mg/mL; the weight ratio of GO to calculated theoretical weight of Fe_3O_4 is equal to 1:0.2) and then stirred for a few hours. Subsequently, the mixture was transferred to a Teflon-lined autoclave and reacted at 180 °C for 12 h to form ethanol-filled intermediate block. After gradual solvent exchange with water and freeze drying, the resultant foams were annealed at 250 and 400 °C for 1 h in argon to obtained T250 and T400 samples, respectively. GFs were fabricated through a similar procedure. The resultant GF was thermal annealed at 250 and 400 °C for 1 h in argon to obtained GF250 and GF400, respectively. The GF without thermal is named GF0.

Measurement of Microwave Absorption Performance. The practical microwave absorption performance was examined based on the Arch method, and four pairs of transmit and receive horn antennas (working at 2−18, 18−26.5, 26.5−40, and 75−110 GHz, respectively) were used. To be specific, the reflectivity of samples in the frequency range of 2−40 GHz was measured on an Agilent PNA-X vector network analyzer (N5244A, 10 MHz to 43.5 GHz). In addition, the reflectivity in the frequency range of 75−110 GHz was measured using an Agilent spectrum analyzer (E4447A, 3 Hz to 42.98 GHz) combined with a PSG Agilent analog signal generator (E8257D, 250 kHz to 40 GHz). To prepare the tested samples, four 3DFGs cut into 90 mm × 90 mm × 10 mm were arranged into a cubic container with internal dimensions of 180 mm × 180 mm × 15 mm for measurements in the band of 2−18, 18−26.5, and 26.5−40 GHz. One 3DFG with the dimension of 90 mm × 90 mm × 10 mm for the measurement in 75−110 GHz. The inside of all cubic containers was paved with 5 mm thick standard aluminum plate to reflect all of the incident microwaves back to the receive antenna. The 3DFG under certain compressive strain was carried out by fixing the sample to the premarked position on the container.

Terahertz Time-Domain Spectroscopy Testing. The time-domain signals of 3DFGs were obtained by a standard four parabolic mirror THz-TDS system. The excitation source is a Ti:sapphire laser with 800 nm wavelength and 75 fs pulse width. THz pulses were generated by a low-temperature grown GaAs photoconductive antenna with a 50 μm slit. The THz beam transmitted through the 3DFGs at normal incidence with a spot diameter of about 2.5 mm. In addition, a ZnTe crystal was used for detection. All of the measurements were carried out at room temperature with the humidity lower than 5%.

Measurement of Electromagnetic Parameter. The relative permittivity and permeability were measured on an Agilent HP8722ES vector network analyzer (VNA) with the coaxial-line method. Typically, the 3DFG was fully soaked in paraffin at 80 °C by vacuum impregnation, and the sample was sanded to 2 mm thickness after cooling down to room temperature. The toroidal standard test sample (3.04 mm i.d., 7 mm o.d.) was fabricated through cutting the 2 mm thickness block with a custom-made annular tool (Figure S24, Supporting Information). The 3DFGs have bulk densities not exceed 2.3 mg cm^{-3} (2.3 mg cm^{-3} for T0, 2.1 mg cm^{-3} for T250 and 1.8 mg cm^{-3} for T400), corresponding to porosities above 99.9%. Therefore, the mass ratios of 3DFGs in 3DFG/paraffin samples with different annealing temperatures of 3DFG are all below 0.27 wt %.

Characterization. The XRD data were obtained through a Rigaku D/Max-2500 diffractometer with Cu Kα radiation. The Raman spectra were recorded on a Renishaw inVia Raman spectrometer using laser excitation at 514.5 nm. XPS measurements were carried out using a PHI 5000 VersaProbe (ULVAC-PHI, Japan). The magnetic hysteresis loops were recorded by a SQUID VSM (Quantum Design, USA) vibrating sample magnetometer. SEM images were taken on a Phenom Pro scanning electron microscope with 10.0 kV accelerating voltage. Atomic emission spectrometry with ICP (ICP−AES) was conducted on an ICP-9000 (N+M) apparatus (Thermo Jarrell-Ash Corp.). The TEM was performed on a FEI Tecnai G2 F20 operating at 200 kV. The Fourier transform infrared spectroscopy was recorded on a Bruker Tensor 27 FT-IR spectrometer. The stress−strain curve was carried out by a home-made Mechanical Tester (BAB-10MT, Transcell Technology Inc.).

■ ASSOCIATED CONTENT

Ⓢ Supporting Information

The Supporting Information is available free of charge on the ACS Publications website at DOI: 10.1021/acsami.8b17654.

> Detailed experimental procedures, including measurement and simulation of microwave absorption performance, terahertz signal processing and calculation of terahertz transmission properties, stress−strain curves, XPS spectra, EDX spectrum, hysteresis loops, detailed TEM and SEM images, simulated RL results, RL curves under different compressive strains, electromagnetic parameters, RL curves after different compression/release cycles, terahertz time-domain spectroscopy, SAMTA values comparison, optical parameters, R_1, R_2 curves and 3D representations of RL curves of 3DFGs, the preparation process of samples for electromagnetic parameter measurement, and comparison of electromagnetic wave absorption performance (PDF)

DOI: 10.1021/acsami.8b17654
ACS Appl. Mater. Interfaces 2019, 11, 1274−1282

AUTHOR INFORMATION

Corresponding Author

*E-mail: yihuang@nankai.edu.cn.

ORCID

Yi Huang: 0000-0001-9343-207X
Shitong Xu: 0000-0001-5552-5566
Yongsheng Chen: 0000-0003-1448-8177

Notes

The authors declare no competing financial interest.

ACKNOWLEDGMENTS

The authors gratefully acknowledge financial support from the MoST (2016YFA0200200), NSFC (21875114, 51373078, and 51422304) of China, Tianjin City (15JCYBJC17700), and 111 project (B18030).

REFERENCES

(1) Lu, X.; Wang, P.; Niyato, D.; Kim, D. I.; Han, Z. Wireless Charging Technologies: Fundamentals, Standards, and Network Applications. *IEEE Commun. Surveys Tuts.* **2016**, *18*, 1413−1452.

(2) Zhang, Y.; Huang, Y.; Zhang, T.; Chang, H.; Xiao, P.; Chen, H.; Huang, Z.; Chen, Y. Broadband and Tunable High-Performance Microwave Absorption of an Ultralight and Highly Compressible Graphene Foam. *Adv. Mater.* **2015**, *27*, 2049−2053.

(3) Micheli, D.; Vricella, A.; Pastore, R.; Marchetti, M. Synthesis and Electromagnetic Characterization of Frequency Selective Radar Absorbing Materials Using Carbon Nanopowders. *Carbon* **2014**, *77*, 756−774.

(4) Singh, P. K.; Korolev, K. A.; Afsar, M. N.; Sonkusale, S. Single and dual band 77/95/110 GHz metamaterial absorbers on flexible polyimide substrate. *Appl. Phys. Lett.* **2011**, *99*, 264101.

(5) Hong, W.; Baek, K.-H.; Lee, Y.; Kim, Y.; Ko, S.-T. Study and Prototyping of Practically Large-Scale Mmwave Antenna Systems for 5G Cellular Devices. *IEEE Commun. Mag.* **2014**, *52*, 63−69.

(6) Song, H.-J.; Nagatsuma, T. Present and Future of Terahertz Communications. *IEEE Trans. Terahertz Sci. Technol.* **2011**, *1*, 256−263.

(7) Watts, C. M.; Liu, X.; Padilla, W. J. Metamaterial Electromagnetic Wave Absorbers. *Adv. Mater.* **2012**, *24*, OP98−OP120.

(8) McIntosh, R. E.; Narayanan, R. M.; Mead, J. B.; Schaubert, D. H. Design and Performance of a 215 GHz Pulsed Radar System. *IEEE. T. Microw. Theory* **1988**, *36*, 994−1001.

(9) Shahzad, F.; Alhabeb, M.; Hatter, C. B.; Anasori, B.; Man Hong, S.; Koo, C. M.; Gogotsi, Y. Electromagnetic Interference Shielding with 2D Transition Metal Carbides (MXenes). *Science* **2016**, *353*, 1137−1140.

(10) Song, W.-L.; Zhou, Z.; Wang, L.-C.; Cheng, X.-D.; Chen, M.; He, R.; Chen, H.; Yang, Y.; Fang, D. Constructing Repairable Meta-Structures of Ultra-Broad-Band Electromagnetic Absorption from Three-Dimensional Printed Patterned Shells. *ACS Appl. Mater. Interfaces* **2017**, *9*, 43179−43187.

(11) Zhang, X.-J.; Wang, G.-S.; Cao, W.-Q.; Wei, Y.-Z.; Liang, J.-F.; Guo, L.; Cao, M.-S. Enhanced Microwave Absorption Property of Reduced Graphene Oxide (RGO)-$MnFe_2O_4$ Nanocomposites and Polyvinylidene Fluoride. *ACS Appl. Mater. Interfaces* **2014**, *6*, 7471−7478.

(12) Liu, J.; Zhang, H.-B.; Sun, R.; Liu, Y.; Liu, Z.; Zhou, A.; Yu, Z.-Z. Hydrophobic, Flexible, and Lightweight MXene Foams for High-Performance Electromagnetic-Interference Shielding. *Adv. Mater.* **2017**, *29*, 1702367.

(13) Han, M.; Yin, X.; Wu, H.; Hou, Z.; Song, C.; Li, X.; Zhang, L.; Cheng, L. Ti_3C_2 MXenes with Modified Surface for High-Performance Electromagnetic Absorption and Shielding in the X-Band. *ACS Appl. Mater. Interfaces* **2016**, *8*, 21011−21019.

(14) Ye, F.; Song, Q.; Zhang, Z.; Li, W.; Zhang, S.; Yin, X.; Zhou, Y.; Tao, H.; Liu, Y.; Cheng, L.; Zhang, L.; Li, H. Direct Growth of Edge-Rich Graphene with Tunable Dielectric Properties in Porous Si_3N_4 Ceramic for Broadband High-Performance Microwave Absorption. *Adv. Funct. Mater.* **2018**, *28*, 1707205.

(15) Wang, G.; Gao, Z.; Tang, S.; Chen, C.; Duan, F.; Zhao, S.; Lin, S.; Feng, Y.; Zhou, L.; Qin, Y. Microwave Absorption Properties of Carbon Nanocoils Coated with Highly Controlled Magnetic Materials by Atomic Layer Deposition. *ACS Nano* **2012**, *6*, 11009−11017.

(16) Hu, D.; Cao, J.; Li, W.; Zhang, C.; Wu, T.; Li, Q.; Chen, Z.; Wang, Y.; Guan, J. Optically Transparent Broadband Microwave Absorption Metamaterial by Standing-up Closed-Ring Resonators. *Adv. Opt. Mater.* **2017**, *5*, 1700109.

(17) Liu, Q.; Cao, Q.; Bi, H.; Liang, C.; Yuan, K.; She, W.; Yang, Y.; Che, R. CoNi@SiO_2 @TiO_2 and CoNi@Air@TiO_2 Microspheres with Strong Wideband Microwave Absorption. *Adv. Mater.* **2015**, *28*, 486−490.

(18) Sun, G.; Dong, B.; Cao, M.; Wei, B.; Hu, C. Hierarchical Dendrite-Like Magnetic Materials of Fe_3O_4, γ-Fe_2O_3, and Fe with High Performance of Microwave Absorption. *Chem. Mater.* **2011**, *23*, 1587−1593.

(19) Tian, C.; Du, Y.; Xu, P.; Qiang, R.; Wang, Y.; Ding, D.; Xue, J.; Ma, J.; Zhao, H.; Han, X. Constructing Uniform Core-Shell PPy@PANI Composites with Tunable Shell Thickness toward Enhancement in Microwave Absorption. *ACS Appl. Mater. Interfaces* **2015**, *7*, 20090−20099.

(20) Li, W.; Jin, H.; Zeng, Z.; Zhang, L.; Zhang, H.; Zhang, Z. Flexible and Easy-to-Tune Broadband Electromagnetic Wave Absorber Based on Carbon Resistive Film Sandwiched by Silicon Rubber/Multi-Walled Carbon Nanotube Composites. *Carbon* **2017**, *121*, 544−551.

(21) Wang, C.; Chen, M.; Lei, H.; Yao, K.; Li, H.; Wen, W.; Fang, D. Radar Stealth and Mechanical Properties of a Broadband Radar Absorbing Structure. *Composites, Part B* **2017**, *123*, 19−27.

(22) Saville, P. *Review of Radar Absorbing Materials*; Defence R&D Canada-Atlantic: Canada, 2005; pp 14−22.

(23) Landy, N. I.; Sajuyigbe, S.; Mock, J. J.; Smith, D. R.; Padilla, W. J. Perfect Metamaterial Absorber. *Phys. Rev. Lett.* **2008**, *100*, 207402.

(24) Liu, S.; Chen, H.; Cui, T. J. A Broadband Terahertz Absorber Using Multi-Layer Stacked Bars. *Appl. Phys. Lett.* **2015**, *106*, 151601.

(25) Ding, F.; Cui, Y.; Ge, X.; Jin, Y.; He, S. Ultra-Broadband Microwave Metamaterial Absorber. *Appl. Phys. Lett.* **2012**, *100*, 103506.

(26) Xin, W.; Binzhen, Z.; Wanjun, W.; Junlin, W.; Junping, D. Design and Characterization of an Ultrabroadband Metamaterial Microwave Absorber. *IEEE Photonics J.* **2017**, *9*, 4600213.

(27) Shen, X.; Yang, Y.; Zang, Y.; Gu, J.; Han, J.; Zhang, W.; Jun Cui, T. Triple-Band Terahertz Metamaterial Absorber: Design, Experiment, and Physical Interpretation. *Appl. Phys. Lett.* **2012**, *101*, 154102.

(28) Shen, B.; Li, Y.; Yi, D.; Zhai, W.; Wei, X.; Zheng, W. Microcellular Graphene Foam for Improved Broadband Electromagnetic Interference Shielding. *Carbon* **2016**, *102*, 154−160.

(29) Feng, J.; Zhang, Y.; Wang, P.; Fan, H. Oblique Incidence Performance of Radar Absorbing Honeycombs. *Composites, Part B* **2016**, *99*, 465−471.

(30) Xi, J.; Zhou, E.; Liu, Y.; Gao, W.; Ying, J.; Chen, Z.; Gao, C. Wood-Based Straightway Channel Structure for High Performance Microwave Absorption. *Carbon* **2017**, *124*, 492−498.

(31) Zhu, Y.; Murali, S.; Cai, W.; Li, X.; Suk, J. W.; Potts, J. R.; Ruoff, R. S. Graphene and Graphene Oxide: Synthesis, Properties, and Applications. *Adv. Mater.* **2010**, *22*, 3906−3924.

(32) Han, J.; Kong, D.; Lv, W.; Tang, D.-M.; Han, D.; Zhang, C.; Liu, D.; Xiao, Z.; Zhang, X.; Xiao, J.; He, X.; Hsia, F.-C.; Zhang, C.; Tao, Y.; Golberg, D.; Kang, F.; Zhi, L.; Yang, Q.-H. Caging Tin Oxide in Three-Dimensional Graphene Networks for Superior Volumetric Lithium Storage. *Nat. Commun.* **2018**, *9*, 402.

(33) Zhang, P.; Li, J.; Lv, L.; Zhao, Y.; Qu, L. Vertically Aligned Graphene Sheets Membrane for Highly Efficient Solar Thermal Generation of Clean Water. *ACS Nano* **2017**, *11*, 5087−5093.

DOI: 10.1021/acsami.8b17654
ACS Appl. Mater. Interfaces 2019, 11, 1274−1282

(34) Qiu, L.; Liu, J. Z.; Chang, S. L.; Wu, Y.; Li, D. Biomimetic Superelastic Graphene-Based Cellular Monoliths. *Nat. Commun.* **2012**, *3*, 1241.
(35) Huang, X.; Qi, X.; Boey, F.; Zhang, H. Graphene-Based Composites. *Chem. Soc. Rev.* **2012**, *41*, 666−686.
(36) Zhang, X. F.; Dong, X. L.; Huang, H.; Lv, B.; Lei, J. P.; Choi, C. J. Microstructure and Microwave Absorption Properties of Carbon-Coated Iron Nanocapsules. *J. Phys. D: Appl. Phys.* **2007**, *40*, 5383−5387.
(37) Che, R. C.; Peng, L.-M.; Duan, X. F.; Chen, Q.; Liang, X. L. Microwave Absorption Enhancement and Complex Permittivity and Permeability of Fe Encapsulated within Carbon Nanotubes. *Adv. Mater.* **2004**, *16*, 401−405.
(38) Fan, Z.; Luo, G.; Zhang, Z.; Zhou, L.; Wei, F. Electromagnetic and Microwave Absorbing Properties of Multi-Walled Carbon Nanotubes/Polymer Composites. *Mater. Sci. Eng., B* **2006**, *132*, 85−89.
(39) Qin, F.; Brosseau, C. A Review and Analysis of Microwave Absorption in Polymer Composites Filled with Carbonaceous Particles. *J. Appl. Phys.* **2012**, *111*, 061301.
(40) Sun, H.; Che, R.; You, X.; Jiang, Y.; Yang, Z.; Deng, J.; Qiu, L.; Peng, H. Cross-Stacking Aligned Carbon-Nanotube Films to Tune Microwave Absorption Frequencies and Increase Absorption Intensities. *Adv. Mater.* **2014**, *26*, 8120−8125.
(41) Chen, H.; Huang, Z.; Huang, Y.; Zhang, Y.; Ge, Z.; Qin, B.; Liu, Z.; Shi, Q.; Xiao, P.; Yang, Y.; Zhang, T.; Chen, Y. Synergistically Assembled MWCNT/Graphene Foam with Highly Efficient Microwave Absorption in Both C and X Bands. *Carbon* **2017**, *124*, 506−514.
(42) Zhang, Y.; Huang, Y.; Chen, H.; Huang, Z.; Yang, Y.; Xiao, P.; Zhou, Y.; Chen, Y. Composition and Structure Control of Ultralight Graphene Foam for High-Performance Microwave Absorption. *Carbon* **2016**, *105*, 438−447.
(43) de Faria, D. L. A.; Venâncio Silva, S.; de Oliveira, M. T. Raman Microspectroscopy of Some Iron Oxides and Oxyhydroxides. *J. Raman Spectrosc.* **1997**, *28*, 873−878.
(44) Sun, X.; He, J.; Li, G.; Tang, J.; Wang, T.; Guo, Y.; Xue, H. Laminated Magnetic Graphene with Enhanced Electromagnetic Wave Absorption Properties. *J. Mater. Chem. C* **2013**, *1*, 765−777.
(45) Lv, H.; Guo, Y.; Yang, Z.; Cheng, Y.; Wang, L. P.; Zhang, B.; Zhao, Y.; Xu, Z. J.; Ji, G. A Brief Introduction to the Fabrication and Synthesis of Graphene Based Composites for the Realization of Electromagnetic Absorbing Materials. *J. Mater. Chem.C* **2017**, *5*, 491−512.
(46) Sareni, B.; Krähenbühl, L.; Beroual, A.; Brosseau, C. Effective Dielectric Constant of Random Composite Materials. *J. Appl. Phys.* **1997**, *81*, 2375−2383.
(47) Bruder, J. A. IEEE Radar Standards and the Radar Systems Panel. *IEEE Aerosp. Electron. Syst. Mag.* **2013**, *28*, 19−22.
(48) Taraskin, S. N.; Simdyankin, S. I.; Elliott, S. R.; Neilson, J. R.; Lo, T. Universal Features of Terahertz Absorption in Disordered Materials. *Phys. Rev. Lett.* **2006**, *97*, 055504.
(49) Lloyd-Hughes, J.; Jeon, T.-I. A Review of the Terahertz Conductivity of Bulk and Nano-Materials. *J. Infrared Millim. Terahertz Waves* **2012**, *33*, 871−925.
(50) Chamorro-Posada, P.; Vázquez-Cabo, J.; Rubiños-López, Ó.; Martín-Gil, J.; Hernández-Navarro, S.; Martín-Ramos, P.; Sánchez-Arévalo, F. M.; Tamashausky, A. V.; Merino-Sánchez, C.; Dante, R. C. THz TDS Study of Several sp^2 Carbon Materials: Graphite, Needle Coke and Graphene Oxides. *Carbon* **2016**, *98*, 484−490.
(51) Huang, Z.; Chen, H.; Huang, Y.; Ge, Z.; Zhou, Y.; Yang, Y.; Xiao, P.; Liang, J.; Zhang, T.; Shi, Q.; Li, G.; Chen, Y. Ultra-Broadband Wide-Angle Terahertz Absorption Properties of 3D Graphene Foam. *Adv. Funct. Mater.* **2017**, *28*, 1704363.
(52) Lott, J.; Xia, C.; Kosnosky, L.; Weder, C.; Shan, J. Terahertz Photonic Crystals Based on Barium Titanate/Polymer Nanocomposites. *Adv. Mater.* **2008**, *20*, 3649−3653.

DOI: 10.1021/acsami.8b17654
ACS Appl. Mater. Interfaces 2019, 11, 1274−1282